Journal of Volcanology and Geothermal Research

191 , 233–244, 2010 **doi:10.1016/j.jvolgeores.2010.02.004**

Depth determinations of shallow hydrothermal systems by self-potential and multi-scale wavelet tomography

Guillaume Mauri[a,b*], Glyn Williams-Jones[a], Ginette Saracco[b]

[a] Department of Earth Sciences, Simon Fraser University, Burnaby, BC, Canada, e-mail : gmauri@sfu.ca
[b]CNRS-CEREGE-UMR6635, Equipe Modelisation , AMU, Université Paul Cézanne, Aix-en-Provence, France, e-mail : ginet@cerege.fr

Article history:
Received 14 April 2009
Accepted 9 February 2010
Available online 16 February 2010

Keywords:
hydrothermal
self-potential
wavelet
volcanoes

A b s t r a c t

In hydrothermal studies, the depth of the hydrothermal system is always required, but rarely known via traditional geophysical exploration techniques. While previous studies have shown that continuous wavelet transform algorithms applied to self-potential data can theoretically determine the depth of the hydrothermal fluids, this study uses multi-scale wavelet tomography with multiple wavelets, field measurements and geophysical models to accurately determine this depth. On Stromboli, Waita and Masaya volcanoes, multi-scale wavelet tomography of field measurements gives reproducible depth results, supported by independent geophysical measurements and models, and accurately locates the main water flow paths at shallow depths. Unlike other traditional geophysical methods, multi-scale wavelet tomography using self-potential data is a low cost tool to rapidly determine depths of the shallowest hydrothermal structures. This approach has the potential to significantly enhance our ability to locate geothermal systems and monitor active volcanoes.

1. Introduction

In volcano monitoring and geothermal exploration, the depth of the hydrothermal fluid is of significant importance in understanding changes in the hydrothermal system and how these changes relate to the underlying magma body. Hydrothermal systems are highly variable in shape and intensity making them difficult to model. Potential field techniques (e.g. gravity, magnetism and self-potential) enable indirect geophysical observations of subsurface structures and are commonly used to infer the horizontal extension of hydro-thermal systems (e.g. *Revil et al, 1999; Battaglia et al. 2006*). However, none of these give accurate depths of the main fluid cells that form the hydrothermal system. To achieve this, we apply signal processing algorithms to potential fields in order to locate the main water flow within volcanoes.

Wavelet transform is a method that allows us to characterize and locate discontinuities or abrupt changes in a measured signal. The depth localization of hydrothermal fluids was first attempted on Piton de la Fournaise volcano (France) by applying multi-scale wavelet tomography (MWT) to self-potential (SP) data using complex wavelets based on the derivative of the Poisson kernel of different orders (Saracco et al., 2004). Our study uses four real wavelets, whose derivative order varies from 2 to 3, and are used separately to determine depths, along a profile, of the main sources generating the potential field measured on the surface (*Moreau et al. 1997, 1999; Fedi & Quarta 1998; Sailhac & Marquis 2001; Sailhac et al. 2000; Gibert & Pessel, 2001; Saracco et al., 2004, 2007*). Due to the difficulties in obtaining good empirical data from exploration drill holes coincident with self-potential surveys in active hydrothermal systems, this study applies MWT to SP data from three volcanoes Stromboli volcano (Italy), Waita volcano (Japan) and Masaya volcano (Nicaragua), for which other independent geophysical data exist (Fig. 1).

2. Self-potential

The self-potential method is a passive electrical technique which allows for measurement of the difference in potential between two points. The electric potential is due to a natural current flowing through the rock, caused by several physical and chemical pheno-mena (*Corwin & Hoover, 1979; Ishido & Mizutani, 1981; Zlotnicki and Nishida 2003; Jardani et al. 2006; Lénat 2007; Aizawa et al.* 2008). On active volcanoes or geothermal areas, self-potential anomalies are typically generated by two main processes. The first is the electrokinetic effect, caused by the displacement of fluid through a porous medium which disrupts the electrical charge balance between polarized minerals and the free ions within the pore fluid. This ionic displacement generates a current that can produce an electric potential of several hundred of mV in amplitude *(Corwin & Hoover 1979; Zlotnicki & Nishida 2003)*. The second source is typically the thermoelectric effect which occurs due to a thermal gradient through the rock (Zlotnicki & Nishida 2003). This

* Corresponding author.
E-mail address: gmauri@sfu.ca (G. Mauri).

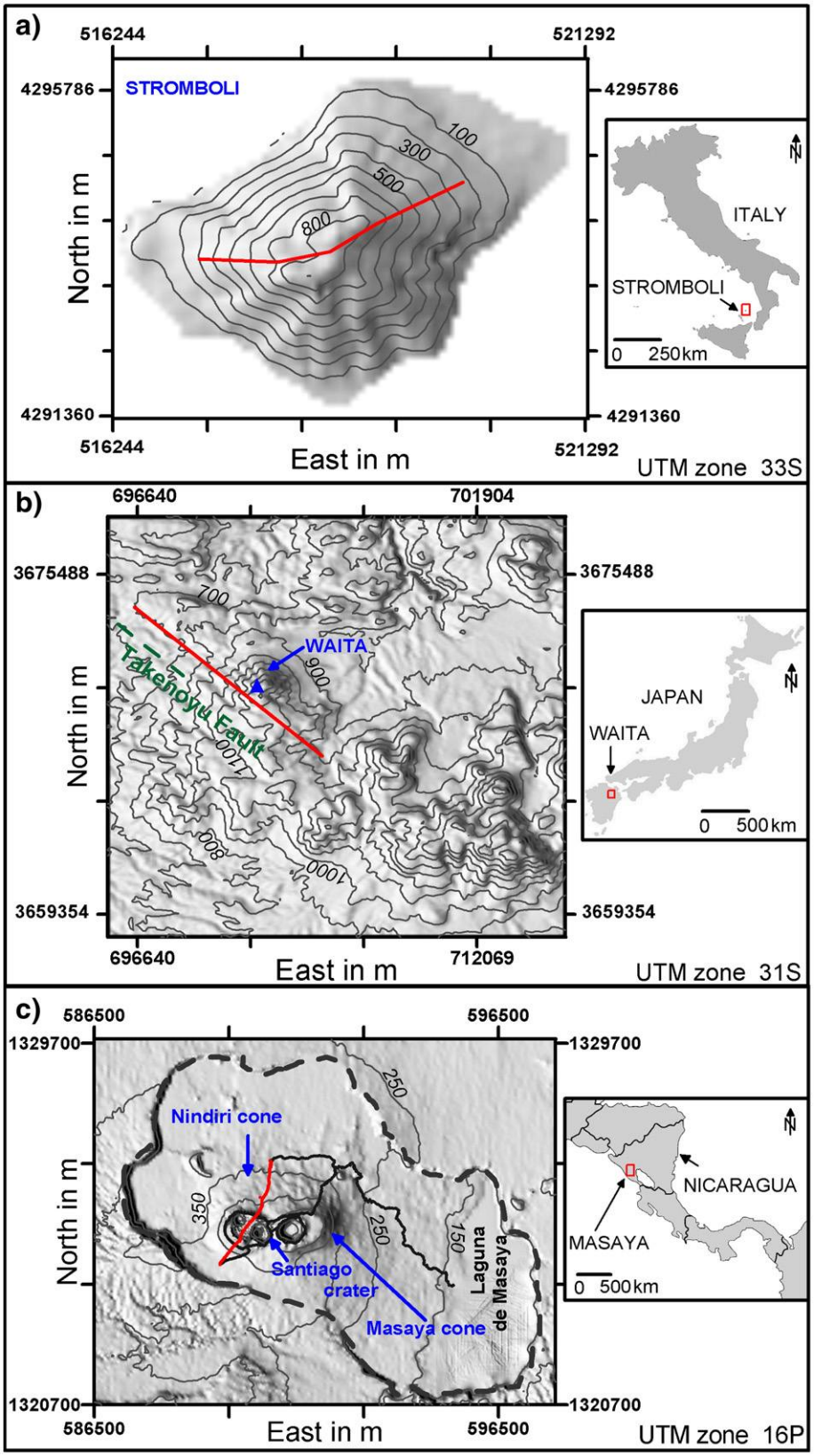


Fig. 1. a) Geographic setting of Stromboli volcano, Italy. Red line is the approximate location of the 2004 SP profile (Finizola et al 2006). b) Geographic setting of Waita volcano, Kyushu Island, Japan. Green dashed line is Takenoyu fault and the red line is the approximate location of the 1995–1996 SP profiles (Yasukawa et al 2003); c) Geographic setting of Masaya volcano, Nicaragua. Black dashed line denotes the caldera margin. Red line is the approximate location of the 2007 and 2008 SP profiles (this study) Contours in m.

thermal gradient increases the energy of the ions leading to a differential displacement between the ions, generating an electrical current. Typically, the associated electric potential is on the order of several tens of mV. Other chemical parameters such as pH and redox reactions will influence current generation (Aizawa et al., 2008), as well as changes in porosity and permeability which control the water flow carrying the ions (Jouniaux et al., 2000).

Heterogeneous ground resistivity may also have an effect on the electric potential measured on the surface (Minsley et al., 2007). Unfortunately it is rarely possible to accurately determine how much the self-potential signal is affected by large underground resistivity contrasts. However, a reasonable first order approximation can be made. On some volcanoes, where underground resistivity is known, previous studies have shown that limits of significant resistivity contrast are associated with the limits of water-saturated rock (Widarto et al., 1992; Revil et al., 2004; Finizola et al., 2006; MacNeil et al., 2007; Barde-Cabusson et al., 2009) or with structural limits (Finizola et al., 2006). For example, in the case of Stromboli volcano, low resistivity layers are associated with underground water and some of the resistivity boundaries are associated with structural boundaries, such as the NeoStromboli crater rim, which acts as a seal and restricts the lateral hydrothermal extension (Finizola et al., 2006). Thus, as a first order approximation, one may assume that the borders of resistivity contrast reflect the borders or the main underground water systems and thus will not affect the self-potential signal in an irreversible way. Consequently, the medium may be assumed to be homogenous. Nevertheless, in order to verify this assumption, a model of a synthetic SP signal in a heterogeneous medium will be analysed and discussed below (Yasukawa et al., 2003; Revil et al., 2004; Finizola et al., 2006; MacNeil et al., 2007).

On active volcanoes and geothermal systems, the electrokinetic and thermoelectric effects are considered to be the most significant source of SP signals (Corwin and Hoover, 1979; Sailhac and Marquis, 2001; Zlotnicki and Nishida, 2003; Revil et al., 2004; Lénat, 2007; Aizawa et al., 2008).

3. Multi-scale wavelet tomography (MWT)

The wavelet transform is a signal analysis method which allows characterization of the time-frequency (spatial position) behaviour of a signal, or characterization and localization of discontinuities in the space and time domain. A full description of continuous wavelet transform (CWT) can be found in the pioneering work of Grossmann and Morlet (1984). Multi-scale wavelet tomography (MWT) is based on CWT and potential field theory, where the calculated depth is obtained by cross-correlating the results from several CWT analyses and where each CWT analysis is made using a different wavelet. The use of wavelets from the Poisson kernel family allows us to obtain a result expressed in depth rather than in frequency. In this study, MWT is used with a combination of four real wavelets of the derivative of the Poisson kernel family (horizontal and vertical derivatives). This Poisson kernel family was developed to investigate the origins of potential fields (Moreau et al., 1997, Sailhac and Marquis, 2001; Sailhac et al., 2000; Gibert and Pessel, 2001; Fedi and Quarta, 1998; Fedi et al., 2004, 2005; Cooper, 2006; Saracco et al., 2004, 2007; Crespy et al., 2008) and is based on the combination of wavelet theory and the dilation property of the Poisson kernel solution of the Laplace equation. Depths are determined from MWT of the potential-field signal, where maxima and minima of extrema lines (amplitude of the wavelet coefficient) converge toward the source generating the measured potential-field. In the case of water flow, the strongest electrical signals are generated at the top of the flow and at the edges between saturated and unsaturated areas Zlotnicki and Nishida (2003)).

In continuous wavelet processing, a singularity (anomaly) from a signal, s, is typically described by a local exponent obtained from the behaviour of the wavelet transform across the range of dilations. In the case of potential fields, the structural order of the source responsible for the measured signal is expressed by the parameter α as a real number (Moreau et al., 1997; Fedi and Quarta, 1998; Sailhac and Marquis, 2001; Sailhac et al., 2000; Saracco et al., 2004, 2007; Crespy et al., 2008). When $\alpha=-1$, the source is a monopole and when $\alpha=-2$, the source is a dipole. However, in most natural cases, the source has a more complex structure, such as a body consisting of both monopoles and dipoles and as such, α will be between -1 and -2. For a singularity with a homogeneous distribution order of $\alpha\leq 0$, the derivative order $n\in\Re^m$ of the wavelet must be $n\geq -(1+\alpha)$. This equation is only true for electrical signals; the relation differs slightly for magnetic or gravity signals (Moreau et al., 1997; Sailhac et al., 2000). If the signal, s, generated by the singularity, confirms the homogeneous property of the wavelet transform (Moreau et al., 1997; Fedi and Quarta, 1998; Sailhac and Marquis, 2001; Sailhac et al., 2000), then the wavelet transform, $L_{(b,a)}$, of the signal, s, by a wavelet, g, is:

$$L_{(b,a)}s = a^{-n}\int g\left(\frac{r-b}{a}\right)s(r)dr^n \qquad \text{with} \quad n\geq -(1+\alpha) \tag{1}$$

where $n\in\Re^m$, b is the translation parameter and a is the dilation parameter. The general equation of the wavelets based on the horizontal derivative of order n of the Poisson kernel family, $H_n(u)$ (Moreau et al., 1997, 1999; Sailhac et al., 2000; Fedi et al., 2005), is in the frequency domain:

$$H_n(u) = (2\pi i u)^n \times \exp\left(-2\pi|u|\right) \tag{2}$$

where the frequency, u, is the Fourier transform of the distance, x, in the frequency domain.

This study also used wavelets based on the vertical derivative order of the Poisson kernel family (Moreau et al., 1997; Sailhac et al., 2000). In the frequency domain, the vertical component does not change. However, as the analysed signal, s, is expressed by u, it is necessary to express the vertical derivative of order n of the Poisson kernel family in the domain frequency using the horizontal component u. One must then apply a Hilbert transform as described in the work of Sailhac et al. (2000) and Saracco et al. (2007). The general equation of the vertical derivative of order n of the Poisson kernel family, $V_n(u)$, in the frequency domain is:

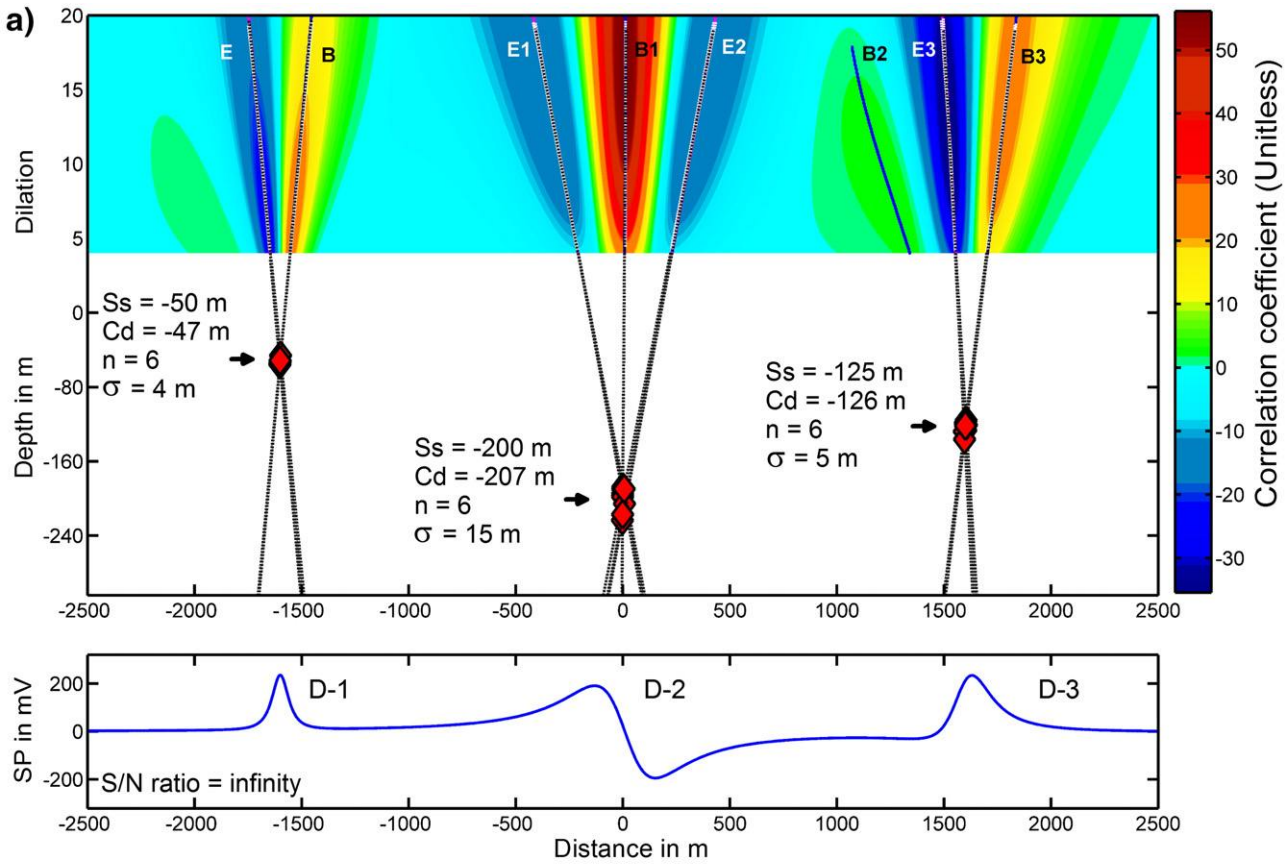
$$V_n(u) = -2\pi|u|(2\pi i u)^{(n-1)} \times \exp\left(-2\pi|u|\right) \tag{3}$$

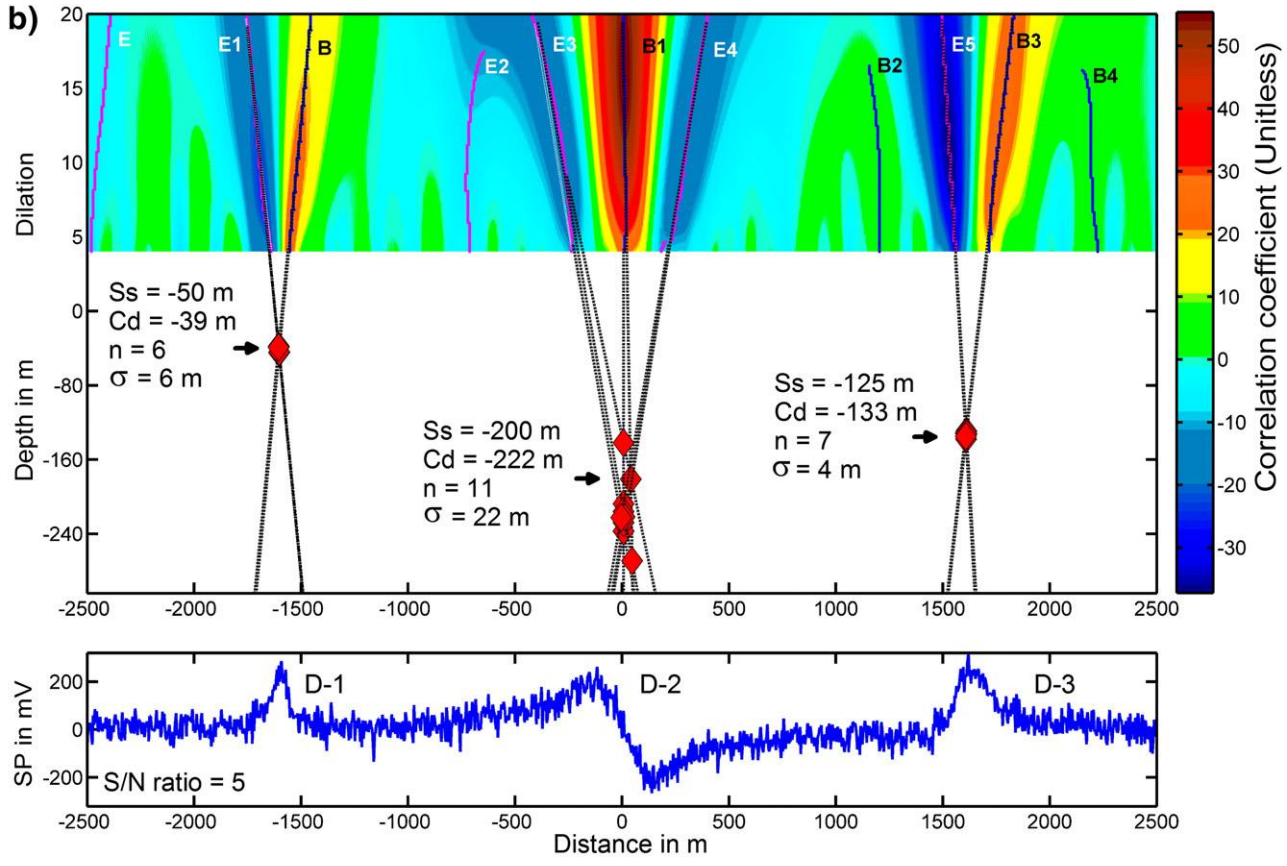
with i being the imaginary number.

Traditionally, continuous wavelet transforms are used over a range of dilations to obtain a multi-scale analysis of the analysed signal. Thus Eq. (1) can be expressed over a range of dilations ($a_{\min}<a<a_{\max}$) and the continuous wavelet transform of signal, s, by the wavelet, g, is $W_{(b,a)}(L,s)$:

$$W_{(b,a)}(L,s) = \int_{a\,\min}^{a\,\max} L_{(b,a)}s\,da \tag{4}$$

The result of Eq. (4), $W_{(b,a)}(L,s)$, is expressed by a matrix of correlation coefficients, which represents, through the continuous wavelet analysis, the expression of the source components making the analysed signal (Grossmann and Morlet, 1984). The matrix of correlation coefficients, $W_{(b,a)}(L,s)$, corresponds to the space above the ground surface ($z_0>0$), however, projection below surface ($x, z<0$) is only possible due to the Poisson kernel properties. Each source can be considered as a singularity, which is defined by at least 2 or more lines of extrema (Fig. 2, lines of minima and maxima) and where at least one line is of maxima and one line is of minima. The lines of


a)
E
B
E1
B1
E2
B2
E3
B3
Dilation
Depth in m
Ss = -50 m
Cd = -47 m
n = 6
σ = 4 m
Ss = -200 m
Cd = -207 m
n = 6
σ = 15 m
Ss = -125 m
Cd = -126 m
n = 6
σ = 5 m
Correlation coefficient (Unitless)
SP in mV
D-1
D-2
D-3
S/N ratio = infinity
Distance in m


b)
E
E1
B
E2
E3
B1
E4
B2
E5
B3
B4
Dilation
Depth in m
Ss = -50 m
Cd = -39 m
n = 6
σ = 6 m
Ss = -200 m
Cd = -222 m
n = 11
σ = 22 m
Ss = -125 m
Cd = -133 m
n = 7
σ = 4 m
Correlation coefficient (Unitless)
SP in mV
D-1
D-2
D-3
S/N ratio = 5
Distance in m

extrema converge (with $z<0$) in a cone shaped structure toward the singularity, which is the mathematical expression of the source, in this case the hydrothermal fluid cell (Moreau et al., 1997; Fedi and Quarta, 1998; Sailhac and Marquis, 2001; Sailhac et al., 2000; Gibert and Pessel, 2001).

The depth determination is thus based on the electric potential equation which can be deduced from Maxwell equations under a quasi-static limit (Saracco et al., 2004). Potential field theory allows us to obtain the Poisson kernel function, where only its derivatives are admissible for wavelet processing (Moreau et al., 1997, 1999). If the potential field in any plane $z_0 = z$ and $z_0 > 0$ is known, then the potential can be calculated in the entire half-space ($z>0$), without any assumptions regarding the sources. This is accomplished through field observations and measurements. A more detailed description of the mathematical methodology can be found in the work of Moreau et al. (1997, 1999), Fedi and Quarta (1998), Sailhac et al. (2000, 2001), Gibert and Pessel (2001), Fedi et al. (2004) and Saracco et al. (2007).

In order to demonstrate the capability of multi-scale wavelet tomography to localize sources, two different models of synthetic self-potential signals have been generated. The first model is a synthetic self-potential signal made from three dipoles at specific depths and orientations. The second model is a synthetic self-potential signal made from one dipole within a heterogeneous medium and beneath a topographic slope of 10°.

3.1. Depth accuracy in a homogeneous medium

In this model, the resistivity of the medium is homogeneous and the synthetic SP signal is generated by 3 dipoles. Each dipole is a rod 20 m in length. The first dipole is oriented horizontally at 50 m depth, the second vertically oriented at 200 m depth and the third dipole is inclined at 45° at a depth of 125 m. Fig. 2a shows the synthetic self-potential signal without noise (signal/noise ratio, SNR, is infinity). In order to simulate a more natural signal, Gaussian noise was added to generate synthetic signals with a SNR of 10 and 5 (10 and 20% noise, respectively; Fig. 2b). In this example, the synthetic SP signal is processed by MWT using the second vertical derivative of Poisson kernel (V2) (Fig. 2, Table 1). Analysis of the synthetic self-potential signal (sampled with a 4 m step) was made with 500 dilations ranging from 4 to 20. The results show good behaviour of the wavelet analysis with the increasing noise (Table 1).

Variations and errors on depth calculations are due to two main sources. First, noise in the data, due to a heterogeneous medium (Sailhac and Marquis, 2001), will distort the lines of extrema for small dilation values and thus will affect the point of convergence, as seen with the synthetic SP signal (Fig. 2, Table 1). The associated error due to the heterogeneous medium is calculated based on the quality of the best fit of the cone shaped structure (Fig. 2). The sampling step also has a significant impact on the measured signal and on how well the signal may characterize the source. This study uses SP data collected with the common sampling steps of 20 or 50 m, which have proven sufficient to obtain reproducible depths. The error due to field measurement noise can be further limited by processing the signal with several wavelets (e.g., 4) in order to statistically constrain a depth.

3.2. Depth accuracy in a non-homogeneous medium

As discussed previously, heterogeneity in subsurface resistivity may be present within the ground (e.g., Stromboli) and be a significant source of electrical generation (Minsley et al., 2007). In order to investigate the effect of heterogeneous ground resistivity on the depth calculations by multi-scale wavelet tomography, a synthetic signal was generated using the mathematical expression of SP generation from a dipole within a heterogeneous medium (Patella, 1997; Revil et al., 2004) (Fig. 3a). Under a continuous topographic slope of 10°, a non-punctual horizontal dipole was placed within a low resistivity medium (50 Ω m), which is itself surrounded by a very high resistivity medium (10,000 Ω m, Fig. 3a). The dipole (10 m high by 60 m long) is made of a grid of 1 m by 1 m punctual dipoles. The upper left corner of the dipole ($X=2000$) is set at 390 m below the topography surface (Fig. 3a) and at constant elevation. The right side of the dipole ($X=2060$ m) is horizontally 40 m from the resistivity contrast limit (green dashed line, Fig. 3a). As the higher resistivity medium is the closest to the surface, its effect on the electrical field will be to reduce and distort the total self-potential signal measured on the surface (solid line, Fig. 3b). The dipole component of the signal is represented by the blue dashed line and the effect of the resistivity contrast is represented by the green dashed line (Fig. 3b). The total synthetic SP signal generated was analysed by the four wavelets (H2, H3, V2, V3) to investigate the effect of the presence of a strong heterogeneous ground (Table 2 and Fig. 4a).

Furthermore, to investigate the effect of noise on the calculated depth, two more signals were generated based on the total SP signal with the addition of 10% and 20% Gaussian noise, respectively (Table 2, Fig. 3c, Fig. 4b, SNR 10 and 5). Finally, to investigate the effect of the depth of dipole on the calculated depth, two similar models were generated with a dipole at $Z=-200$ m and -100 m, respectively (Table 2). An example of this analysis is presented on Fig. 4, with the dipole at $Z=-390$ m without noise (Fig. 4a) and with 20% noise (SNR 5, Fig. 4b). For each wavelet applied on each depth of the dipoles, the multi-scale wavelet tomography results show that resistivity contrast does not significantly affect the capacity of the wavelet to locate the dipole ($4<\sigma Z<14$ m, Table 2) when no noise was present (SNR = infinity). With the increase in Gaussian noise (from SNR infinity to 5), the depth accuracy of individual wavelet analyses decreases above 10% noise. At SNR of 10, the uncertainty, σZ, is

Table 1
Synthetic source depths and position calculated by MWT of synthetic self-potential signals generated by 3 dipoles with different orientations and depths. The synthetic source (Ss) is the reference depth (Z) and position (X) used to generate the synthetic self-potential signal. Cd is the depth calculated by multi-scale wavelet tomography with the wavelet V2, n is the number of solutions for Cd and σ is one standard deviation. A signal/noise ratio (SNR) of infinity, 10 and 5 was applied to the synthetic self-potential signal to investigate noise effects on the calculated depths. Distance along profile (X) and depth (Z) are in m.

	SNR	n	X	σX	Z	σZ
D-1: dipole at 0°						
Ss	–	–	−1600	–	−50	–
Cd	∞	6	−1601	2	−47	4
Cd	10	8	−1601	3	−46	5
Cd	5	6	−1602	4	−39	6
D-2: dipole at 90°						
Ss	–	–	0	–	−200	–
Cd	∞	6	4	10	−207	15
Cd	10	10	18	8	−220	15
Cd	5	11	17	18	−222	25
D-3: dipole at 45°						
Ss	–	–	1600	–	−125	–
Cd	∞	6	1602	5	−126	5
Cd	10	8	1608	2	−125	6
Cd	5	7	1609	2	−133	4

Fig. 2. Calculated depths of three theoretical dipoles at different depths (Z) and orientations (see text and Table 1). From left to right: D-1) horizontal dipole at $Z=-50$ m; D-2) vertical dipole at $Z=-200$ m; D-3) dipole with a 45° dip at $Z=-125$ m. Multi-scale wavelet tomography results with the second derivative (V2) of the Poisson kernel over 500 dilations on a range from 4 to 20. a) Result for a signal without noise. b) Results with a signal/noise ratio of 5. Top: B to B4 and E to E5 represent maxima and minima lines, respectively. Middle: cone shaped structures with intersects at the depth of each source. Bottom: synthetic self-potential signal generated by the three dipoles. Ss is the synthetic source depth, Cd is the calculated depth, n is the number of solutions for Cd and σ is one standard deviation.

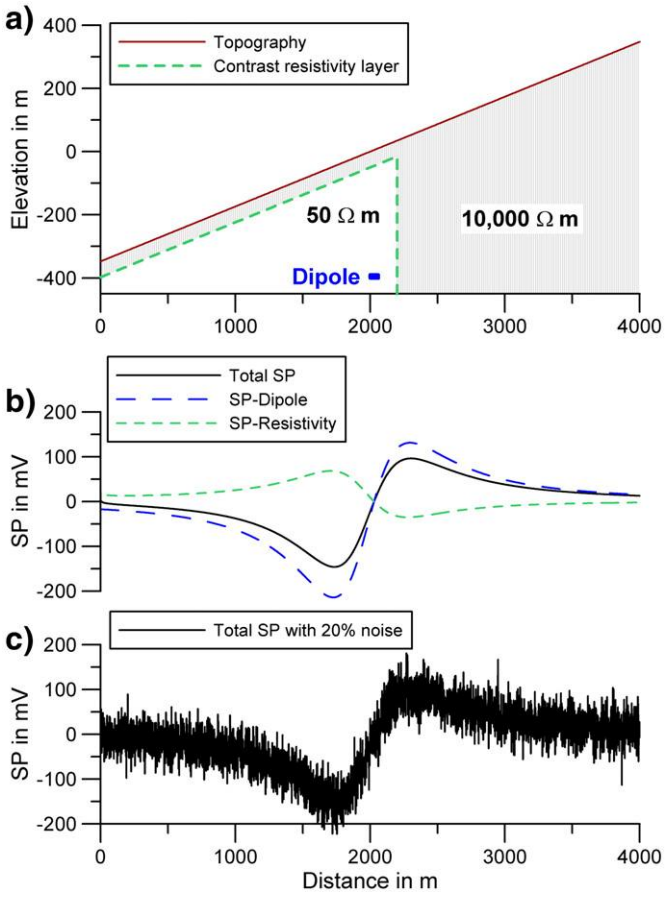


Fig. 3. 2-D model of a synthetic self-potential signal generated by a dipole (D-4) in an non-uniform medium, which is affected by a 20% noise (SNR=5). Sampling step of the grid is 1m.a) Model used to generate the self-potential signal. Topography is a slope of 10. The contrast resistivity layer represents the interface between the two mediums of differing resistivity. The dipole (blue rectangle), is oriented horizontally (10m × 60m) and its depth is defined by its upper left corner (390m below the topographic surface) and bottom left corner (400m below the topographic surface). b) Synthetic self-potential signal associated with the model. The blue dashed line is the SP signal generated by the dipole. The green dashed line is the effect of the contrast resistivity layer. The solid black line represents the total SP signal. c) Total SP signal presented In b) with a 20% Gaussian noise (SNR=5).

Table 2
Synthetic source depths and position calculated by MWT of synthetic self-potential signals generated by a horizontal dipole (D-4) at 3 depths and in a non-homogeneous medium (see Fig.3 and text). Synthetic source (Ss) shows the depth and position of the dipole. Cd is the depth calculated by the multi-scale wavelet tomography with each of the four wavelets H2, H3, V2, V3 (see text), n is the number of solutions for Cd and σ is one standard deviation. A signal/noise ratio (SNR) of infinity, 10 and 5 was applied to the synthetic SP signal to investigate noise effects on the calculated depth. Distance along profile (X) and depth (Z) are in m.

Wavelet	Dipole at 0°	SNR	n	X	σX	Z	σZ
–	Ss	–	–	2000 to 2060	–	−100 to −110	–
H2	Cd	∞	25	2003	5	−115	12
V2	Cd	∞	10	2005	3	−114	10
H3	Cd	∞	12	2004	4	−118	4
V3	Cd	∞	8	2009	6	−112	9
H2	Cd	10	14	2003	4	−116	17
V2	Cd	10	19	2005	11	−107	18
H3	Cd	10	13	2014	19	−114	34
V3	Cd	10	16	2010	5	−120	15
H2	Cd	5	19	2007	4	−131	12
V2	Cd	5	8	2000	11	−109	26
H3	Cd	5	14	2029	9	−89	10
V3	Cd	5	12	2016	6	−149	22
–	Ss	–		2000 to 2060	–	−200 to −210	–
H2	Cd	∞	11	1990	4	−200	10
V2	Cd	∞	8	1984	6	−213	8
H3	Cd	∞	9	1986	4	−207	8
V3	Cd	∞	12	1985	6	−215	7
H2	Cd	10	13	1996	7	−220	20
V2	Cd	10	9	1989	37	−103	28
H3	Cd	10	8	1932	8	−190	17
V3	Cd	10	12	2026	8	−205	21
H2	Cd	5	10	1982	15	−209	25
V2	Cd	5	11	1942	8	−92	17
H3	Cd	5	14	1937	9	−176	33
V3	Cd	5	12	2052	8	−186	22
–	Ss	–		2000 to 2060	–	−390 to −400	–
H2	Cd	∞	12	1958	6	−401	12
V2	Cd	∞	17	1964	12	−391	14
H3	Cd	∞	10	1956	3	−402	4
V3	Cd	∞	8	1960	2	−400	8
H2	Cd	10	6	1972	8	−282	17
V2	Cd	10	8	1841	9	−237	28
H3	Cd	10	7	1900	11	−399	39
V3	Cd	10	14	1965	11	−397	34
H2	Cd	5	7	1950	26	−361	57
V2	Cd	5	20	1867	32	−357	103
H3	Cd	5	10	1815	17	−411	50
V3	Cd	5	12	1991	11	−365	38

between 12 and 39 m while at SNR of 5 the depth uncertainty can reach 103m for a dipole at Z=−390m (Table 2). Although the uncertainty for a given wavelet analysis increases with both depth of the dipole and increasing noise, the resistivity contrast alone does not significantly affect the depth calculation by any of the 4 wavelets. A similar pattern is found on the horizontal uncertainty σX; at Z = -100 with SNR from infinity to 5, all wavelets accurately locate the dipole (Table 2).

Thus, for a dipole at Z=−100m generating a signal with and without noise (SNR=infinity to 5), when the calculated depth is based on the four wavelets, both horizontal and vertical accuracies are good (X=1% error, Z<6% error; Table 3). While the accuracy of the MWT decreases at greater depths (Z=−200m and −390m) the results are nevertheless significantly better than analyses made using only a single wavelet. Therefore, based on modelling of a synthetic signal, the presence of large resistivity contrasts (3 orders of magnitude between the two mediums) or a moderate slope (10°) do not by themselves significantly affect the calculated depth by multi-scale wavelet tomography. Rather, the main parameters responsible for decreasing depth accuracy are the noise affecting the signal and the depth of the source.

In the case of the three volcanoes investigated here (Fig.1), previous studies on both Stromboli (*Revilet al 2004*) and Waita volcanoes (*Yasukawa et al 2003*) have shown that SP signals are principally due the electrokinetic effect, which is commonly assumed to have dipolar behaviour. On Waita volcano, Widarto et al. (1992) have shown that the resistivity contrast is 2 orders of magnitude and ground resistivity is less than 300 Ωm. On Stromboli volcano, the resistivity contrast ranges between 2 and 3 orders of magnitude and are generally less than 3000 Ω m (*Finizola et al. 2006*). Furthermore, these studies have shown that the main subsurface resistivity changes were

Fig. 4. Calculated depths of a non-punctual horizontal dipole at a depth of 390 m (see text, Fig.3 and Table 2). Multi-scale wavelet tomography results with the third vertical derivative (V3) of the Poisson kernel over 600 dilations on a range from 15 to 41. *a)* Results for a signal without noise (SNR=infinity). *b)* Result with a signal/noise ratio of 20% (SNR=5) ; Top: B00 to B02 and E00 to E02 represent maxima and minima lines, respectively. Middle : cone shaped structures with intersects at the depth of each source. Bottom: Synthetic self-potential signal generated by the dipole and affected by the resistivity contrast layer along a topographic slope of 10°, with SNR of infinity (a) . and 5 (b) ; Ss is the synthetic source depth, Cd is the calculated depth, n is the number of solutions for Cd and σ is one standard deviation.

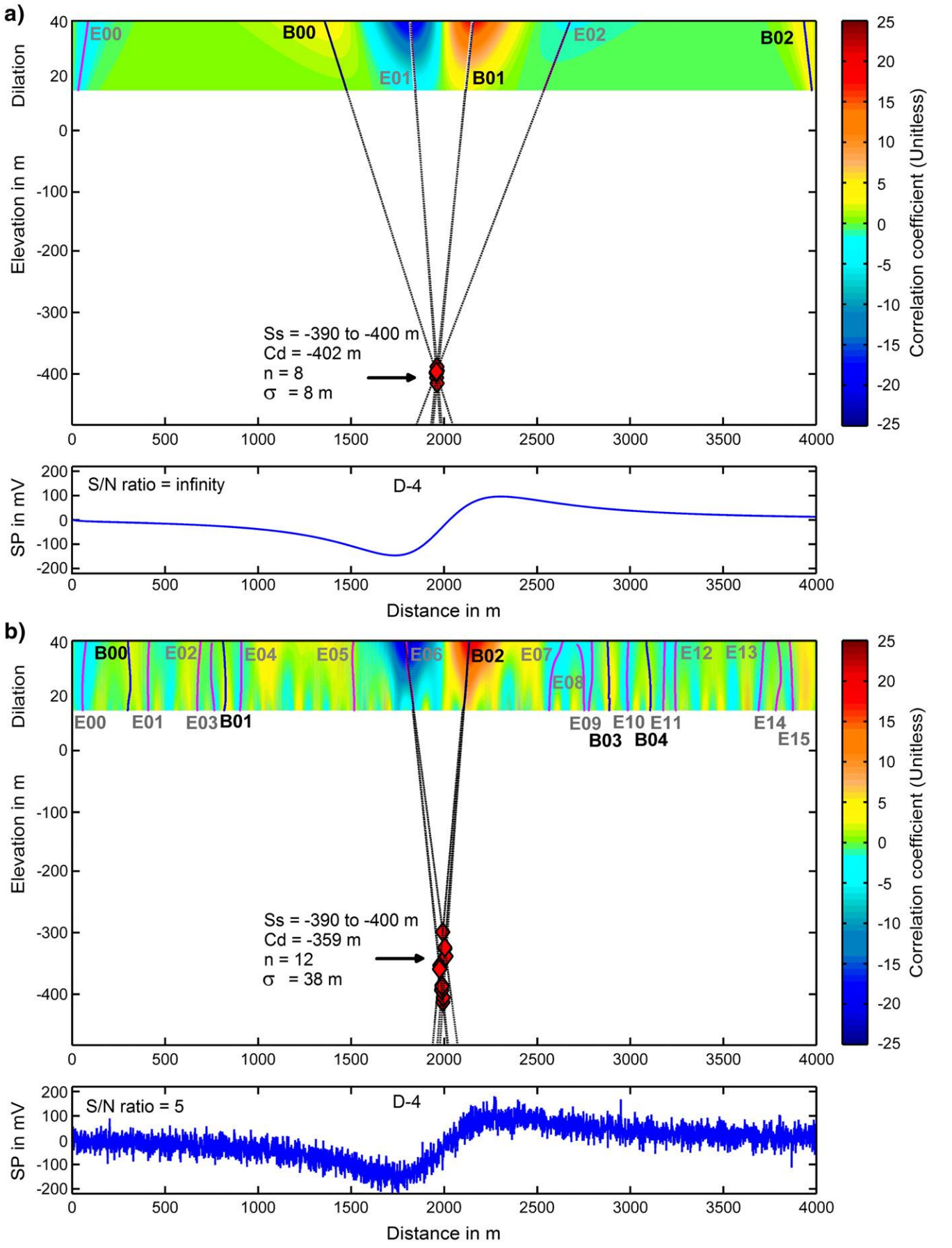

a)
Dilation
Elevation in m
E00
B00
E01
B01
E02
B02
Ss = -390 to -400 m
Cd = -402 m
n = 8
σ = 8 m
Correlation coefficient (Unitless)
SP in mV
S/N ratio = infinity
D-4
Distance in m
b)
B00
E02
E04
E05
E06
B02
E07
E08
E12
E13
E00
E01
E03
B01
E09
E10
E11
B03
B04
E14
E15
Ss = -390 to -400 m
Cd = -359 m
n = 12
σ = 38 m
S/N ratio = 5
D-4

Table 3
Synthetic source depths calculated by multi-scale wavelet tomography of a synthetic self-potential signal of a horizontal dipole (D-4) in a non-homogeneous medium (see Fig. 3 and text). Synthetic source (Ss) shows the depth (Z) and position (X) of the dipole. Cd is the mean depth of all multi-scale wavelet tomography analyses using 4 wavelets H2, H3, V2 and V3 (see text), n is the number of solutions for Cd and σ is one standard deviation. The % error represents the difference between the mean depth and the center of the synthetic dipole source. A signal/noise ratio (SNR) of infinity, 10 and 5 was applied to the synthetic SP signal to investigate noise effects on the calculated depth. Distance along profile (X) and depth (Z) are in m.

D-4	SNR	n	X	σX	% error X	Z	σZ	% error Z
Ss	–	–	2000–2060	–	–	−100 to −110	–	–
Cd	∞	55	2004	6	1±2	−106	14	1±13
Cd	10	62	2008	12	1±1	−105	21	0±20
Cd	5	53	2014	13	1±1	−111	28	6±27
Ss	–		2000–2060	–	–	−200 to −210	–	–
Cd	∞	40	1975	23	3±3	−204	12	0±6
Cd	10	42	1991	37	2±2	−179	49	13±24
Cd	5	47	1988	56	2±3	−189	28	8±14
Ss	–		2000−2060	–	–	−390 to −400	–	–
Cd	∞	47	1960	8	3±4	−397	12	1±4
Cd	10	35	1925	54	5±6	−347	73	12±19
Cd	5	49	1899	71	6±7	−381	79	4±20

associated with the boundary of underground water flow and so their effects on self-potential generation can be included with the effect of water flow. On Masaya volcano, the resistivity contrast (2 orders of magnitude, maximum apparent resistivity 10,000 Ωm) is associated with the upper edge of the water table (*MacNeil et al. 2007*). For the purposes of this study, one can therefore assume a simplified homogeneous medium for each of the volcanoes. Previously published models on each volcano will also allow us to investigate and constrain the significance of depths calculated by MWT of self-potential data.

4. Geologic setting

4.1. Stromboli volcano

Stromboli is an island stratovolcano, located in the Tyrrhenian Sea, Italy (38.178°N, 15.212°E) (Fig 1a). It forms the northernmost part of the Aeolian archipelago and is one of the world's most active volcanoes, with persistent eruptive activity for at least the last 2000 years (*Gillot & Keller 1993*). The sub-aerial history of Stromboli volcano commenced ~100,000 years ago (*Hornig-Kjarsgaard et al. 1993*) and has since led to a strong structural morphology, mainly controlled by a regional NE–SW trend of dyke injection (*Pasquaré et al. 1993*). The volcanic stratigraphy of Stromboli is principally composed of pyroclastic ash and scoria deposits and the main hydrothermal system is located in the summit area (T_{ground} ~80°C, $CO_{2\ gas\ flux}$ ~10,000g m^{-2} d^{-1}, self-potential anomaly ~250 mV in amplitude). Stromboli shows a wide range of ground resistivity (<100 Ωm to >3000 Ωm) and previous self-potential studies correlate the structural boundaries with the extension of the complex hydrothermal system within the volcano (*Finizola et al. 2002, 2003, 2006; Revil et al 2004*). This study uses a self-potential profile acquired in May 2004 across the volcano (NE–SW), 3820 m in length with a sampling step of 20m (Figs. 1a and 5) and a signal/noise ratio of 10. The SP profile was complimented by a resistivity profile, ground temperature and soil CO_2 flux measurements (*Finizola et al., 2006*).

4.2. Waita volcano

Waita volcano is located in the central part of Kyushu Island, Southern Japan (33.140°N, 131.165°E) (Fig. 1b), in the western part of Hohi Geothermal Region (HGR) (*Yasukawa et al. 2003*). Waita volcano is situated within the Beppu–Shimabara Graben (*Kamata, 1989*) and the main fault structures are related to Takenoyu fault (normal fault, oriented NW–SE), while secondary normal faults are oriented EW (*Ikeda, 1979*). Important hydrothermally altered deposits are spread along the Takenoyu fault, suggesting an important fault-controlled flow path (Yasukawa et al. 2003). Waita volcano hosts more than 20 hot springs (ranging from 36.5 to 97.8 °C) and total hot water discharge is estimated at 524 l min^{-1} with the total heat discharge reaching 1352 $kJ\ s^{-1}$ (*Kawamura, 1985*). Previous studies of the hydrothermal system have shown that hydrothermal fluids are rising from depth under Waita volcano and mixing with meteoric water flowing from the top of the volcanic edifice (*Widarto et al., 1992; Yasukawa et al., 2003*). The hydrothermal fluids then flow laterally westwards inside the volcanic edifice along the Takenoyu

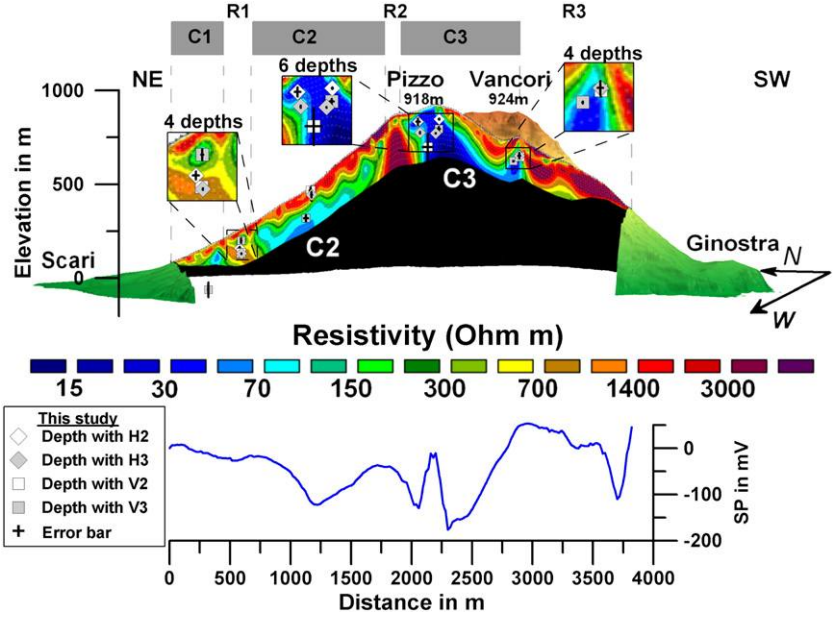


Fig. 5. Top: Comparison between MWT-calculated depths of hydrothermal fluids (squares and diamonds) and the electrical resistivity model (from Finizola et al., 2006) with the self-potential profile across Stromboli volcano, Italy (See Fig. 1a). V2, V3, H2 and H3 are second and third order of the vertical and horizontal derivatives. Error bars represent one standard deviation, see Table 4. Modified from Finizola et al. (2006).

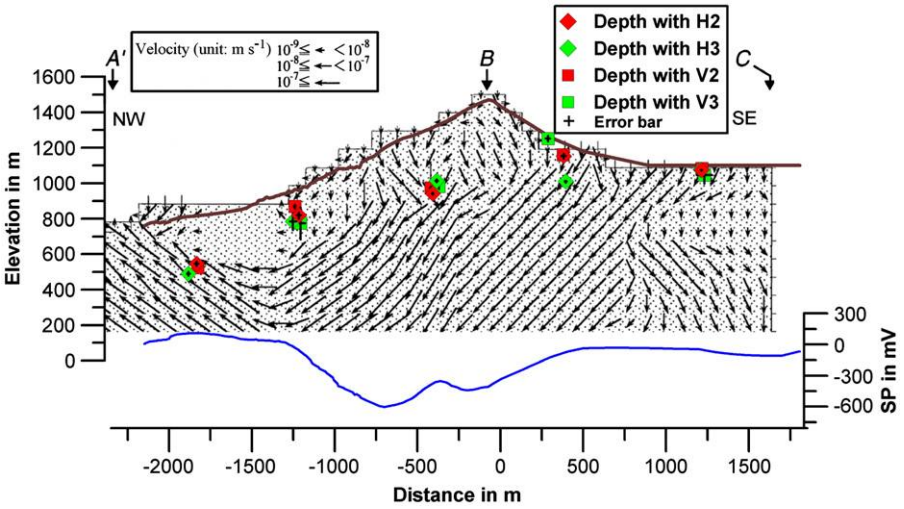


Fig.6. Comparison between MWT-calculated depths of hydrothermal fluids (squares and diamonds) and the fluid velocity distribution model (Model 3, case 2, from Yasukawa et al (2003)) with the self-potential profile (A′–B–C) of Waita volcano, Japan (see Fig. 1b). V2, V3, H2 , H3 are second and third order of the vertical and horizontal derivatives. Error bars represent one standard deviation, see Table 4. Modified from Yasukawa et al. (2003).

fault.The self-potential profile used in this study is oriented NW–SE across the summit of Waita volcano and was made in 1995 and 1996 (*Yasukawa et al 2003*). The SP data consists of a 2000m long profile with a sampling step of 50m and a 1600m long segment based on forward modelling *(Yasukawa et al. 2003*) (Figs. 1b and 6) and has a signal/noise ratio (SNR) of 100 (1% noise). Rock resistivity along the profile ranges from 1 to 300 Ωm (*Widarto et al 1992; Yasukawa et al 2003*).

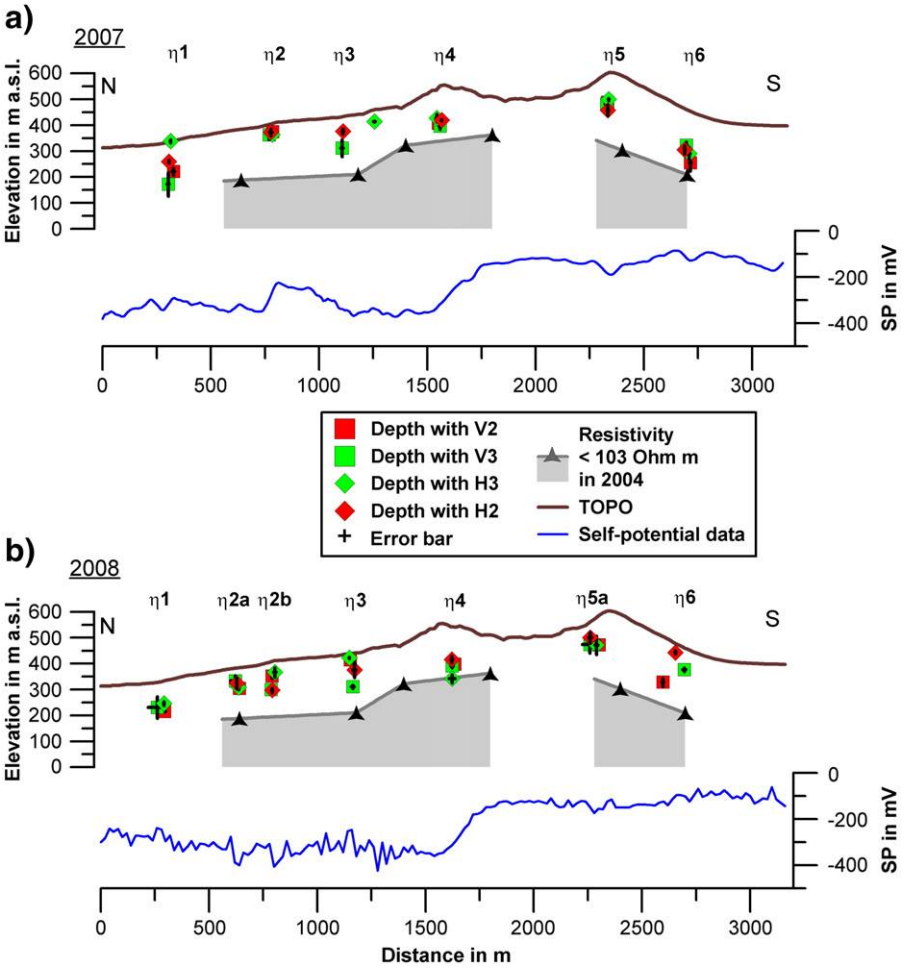


Fig.7. Comparison between the MWT-calculated depths of water table (squares and diamonds) and the TEM water table model (from MacNeil et al. (2007)) with the self-potential profile of Masaya volcano, Nicaragua (see Fig.1c). V2, V3, H2 and H3 are second and third order of the vertical and horizontal derivatives. Error bars represent one standard deviation, see Table 4 and Table 5.

4.3. Masaya volcano

Masaya volcano is located in southwestern Nicaragua (11.984°N, 86.161°W), Central America, about 20 km south of the capital, Managua. Masaya is a basaltic shield volcano (Fig. 1c) with a summit caldera structure (6 km by 11.5 km) (Williams, 1983). Post-caldera activity is largely dominated by intra-caldera effusive eruptions and only small volumes of scoria and ash fall interlayered between lava flows; a complete stratigraphic description can be found in Williams (1983). Recent eruptive centers are spread along an annular structure, which is cut on its eastern part by the Cofradrias fault (Williams, 1983; Walker et al., 1993). The main cones are Masaya, Nindiri, Cerro Montoso, and Comalito (Fig. 1c). For the last ~150 years, volcanic activity has been centered on Santiago crater (eastern part of Nindiri cone) and dominated by persistent open vent degassing, infrequent lava lake formation and small vent-clearing explosions (e.g., Rymer et al., 1998; Roche et al., 2001; Williams-Jones et al., 2003).

Previous geophysical studies with transient electromagnetic methods (TEM) have shown that the north flank of Nindiri cone hosts a shallow water table while the south flank hosts an underground vapour dominated zone (MacNeil et al., 2007), which likely represents a small hydrothermal system. Two self-potential profiles were collected across the Nindiri cone in 2007 and 2008 (this study, Figs. 1c and 7), with a sampling step of 20 m. The signal/noise ratio of this Nindiri profile was ~100 (1% noise) in both 2007 and 2008. All data are referenced to the Laguna de Masaya via a SP mapping survey more than 15 km in length. On Nindiri, self-potential profiles (2007 and 2008) also show the presence of two distinct structures. An extended positive SP anomaly (~200 mV), coincident with the vapour dominated water body (MacNeil et al., 2007), is interpreted as the expression of a small hydrothermal system located on the south flank of Nindiri cone and within Nindiri crater (Fig. 7). The positive self-potential anomaly is independent of the topographic variation (blue profiles on Fig. 7), which is typically a sign of uprising fluid and thus hydrothermal activity. Through the north flank of Nindiri cone, a water table flows northward and is characterized by a low self-potential anomaly (~100 mV), which is controlled by topographic change (SP/elevation gradient from −0.18 to −0.80 mV m^{-1}, Fig. 7).

5. Results

In order to investigate the accuracy of multi-scale wavelet tomography calculated depths of hydrothermal fluids, this study uses a combination of 4 real wavelets based on the Poisson kernel function: the second and third vertical derivative (V2 and V3, respectively, Eq. (3)) and second and third horizontal derivative (H2 and H3, respectively, Eq. (2)). Water flow is generally considered to have a dipolar behaviour ($\alpha = -2$), which in the case of an extended source can be considered as 2 monopoles ($\alpha = -1$) (Sailhac and Marquis, 2001). Using Eq. (1), the wavelets (second and third derivatives) have an order of homogeneous distribution of $n = 2$ and $n = 3$. Each analysis, for each data set, was made with each wavelet over 500 dilations with a range of dilation from 1 to 20. Only depths found with at least three of the four wavelet analyses are considered significant. For each wavelet and each profile, a depth estimate is obtained by calculating the best fit of the cone shaped structure (Fig. 2). For each depth estimate, the associated error is based on the quality of the best fit. The final localization of each source (horizontal and vertical) is based on the mean depth of all solutions from all wavelets analysed and their associated uncertainty (σ). Results for the three volcanoes are synthesised in Table 4.

As discussed previously, noise may be a source of error in the depth calculation. Calculated signal/noise ratios on SP profiles for both Waita and Masaya (2007 and 2008) volcanoes are 100, while the SNR of the SP profile of Stromboli volcano is 10. Even with a SNR as low as 5, for a homogeneous medium, the MWT-calculated depths from the synthetic SP profile (Fig. 2, Table 1) show uncertainties less than 25 m. For a non homogeneous medium (Fig. 4, Table 3), the vertical error is less than 6% for a SNR up to 5. As the noise on the SP profile of both Waita and Masaya volcano is greater than 10, the effect of noise on the calculated depth should be negligible. For Stromboli volcano (SNR = 10), the error due to noise should be less than 50 m for depths less than 200 m. Therefore, the error due to noise on the calculated depths from the three volcanoes is considered to be negligible on Masaya and Waita volcanoes and reasonable for Stromboli volcano.

Table 4
Source depths calculated by multi-scale wavelet tomography of self-potential profiles on Stromboli, Waita and Masaya volcanoes. Number of wavelets used in MWT calculations to locate the source depths and position along profile. Distance along profile (X), depth (Z) and elevation are in m. σ is one standard deviation. *Structure names from Finizola et al. (2006).

Structure	Wavelets	X	σX	Z	σZ	Elevation a.s.l
Stromboli volcano, Fig. 5						
C2*	4	1160	22	−66	26	427
	2	2060	10	−80	38	806
C3*	4	2200	43	−130	46	788
	4	2880	25	−105	17	643
R1*	4	590	7	−184	62	105
Waita volcano, Fig. 6						
# 1	3	−1850	27	−295	30	520
# 2	4	−1230	25	−150	58	815
# 3	4	−400	19	−400	19	920
# 4	4	365	42	−100	76	1135
# 5	4	1220	21	−30	20	1070
Masaya volcano in 2007, Fig. 7a						
1	4	310	7	−116	67	237
2	4	780	8	−40	11	368
3	4	1150	66	−111	46	347
4	3	1560	11	−98	21	406
5	4	2330	6	−131	26	481
6	4	2700	11	−156	31	294
Masaya volcano in 2008, Fig. 7b						
1	3	283	16	−100	30	231
2a	4	632	8	−65	20	318
2b	4	794	7	−79	32	330
3	4	1160	10	−69	52	371
4	4	1626	8	−154	29	388
5	4	2278	20	−92	32	443
6	3	2649	43	−105	60	385

On Stromboli volcano, multi-scale wavelet tomography of the 2004 SP profile identified 18 different depths, in 5 groups (Fig. 6, Table 4) that characterize 5 sources: 5 depths from H2, 5 depths from H3, 4 depths from V2 and 4 depths from V3. Each of these 5 sources covers a distinct area which is horizontally less than 80 m wide and vertically spread over 35 to 150 m (Table 4).

On Waita volcano, the multi-scale wavelet tomography of the 1995–1996 SP profile identified 19 different depths, from 5 sources (Fig. 6, Table 4): 5 depths from H2, 5 depths from H3, 5 depths from V2 and 4 depths from V3. Each of these 5 sources covers a distinct area which is horizontally less than 50 m wide and vertically spread over 40 to 150 m (Table 4).

On Masaya volcano, across the active Nindiri cone, multi-scale wavelet tomography of the 2007 and 2008 SP profiles identified 23 and 26 different depths, respectively, from 6 sources (Fig. 7, Table 4). In 2007, 6 depths are from H2, 6 depths are from H3, 5 depths are from V2 and 6 depths are from V3. The 2007 depths are spread over 6 different locations (η1 to η6, Fig. 7a). In 2008, 6 depths are from H2, 6 depths are from H3, 7 depths are from V2 and 7 depths are from V3. The 2008 depths are organized in 7 groups (η1, η2a, η2b, η3, η4, η5, η6, Fig. 7b). The horizontal and vertical positions of the each of the 5 groups (η1, η3, η4, η5, η6, Fig. 7) are very similar. Between 2007 and 2008, the only

difference is for the source η2 (Table 4, Fig. 7); in 2008, two sources, η2a and η2b, were located in proximity to η2 ($\Delta x_{\eta 2a-\eta 2} = 148$ m, $\Delta z_{\eta 2b-\eta 2} = 50$ m; $\Delta x_{\eta 2b-\eta 2} = 14$ m, $\Delta z_{\eta 2b-\eta 2} = 38$ m). As both η2a and η2b sources where calculated with 4 wavelets and are only 12 m vertically from each other (Table 4), we consider them as equivalent to the η2 source.

6. Discussion

On Stromboli volcano, previous studies (Finizola et al., 2002, 2003, 2006) have shown the presence at shallow depth, from NE to SW, of three conductive structures (C1, C2 and C3) and three resistive structures (R1, R2, R3) (Fig. 5). Our MWT results show 5 sources at relatively shallow depths (from 60 to 300 m) below the topographic surface with almost all located within the low resistivity regions (Fig. 5, Table 4): one source is in the C2 conductive structure, three sources in the C3 structure and one source is inside the R1 resistive structure. Strong correlations between SP, ground temperature, soil CO_2 concentrations and electrical tomography support the existence of strong hydrothermal activity (C3) on the summit of the volcano (Finizola et al., 2006) (Fig. 5).

The depths calculated by MWT correlate very well with the electrical tomography anomalies (Fig. 5) and show the presence of 3 shallow sources inside the C3 structure (Fig. 5). Two sources are located on the summit and a third is on the upper SW flank. Thus, the two shallow sources (60 to 130 m below the topographic surface) likely characterize the main hydrothermal fluid cells (Fig. 5, Table 4) that shape the summit hydrothermal system (C3) of Stromboli. Similar correlations are seen with the calculated depths in the C2 conductive structures (Fig. 5, Table 4). This study also found one source (with each of the four wavelets) within the R1 resistive structure (Fig. 5). In R1, there is a small low resistivity anomaly at shallow depth, embedded in a high resistivity background (Finizola et al., 2006). This low resistivity area is only correlated with high CO_2 concentrations (> 4000 ppm) and its origin is associated with a highly vegetated area in this part of the island. However, given the four MWT-derived depths found for this source and the high CO_2 background concentrations, the R1 structure may represent an area of low-level hydrothermal activity surrounded by less permeable deposits.

On Waita volcano, the 5 groups of calculated depths also characterize five sources (#1 to #5, section A′–B on Fig. 6, Table 4) and correlate with the main flow structures defined by Yasukawa et al. (2003). From left to right on this section, the first source (#1, Table 4) correlates with the upper part of the western water flow (Fig. 6). The second source (#2) is at the edge of the water flow with an impermeable layer. While the flow is not intense, the differential displacement is clearly sufficient to generate an electrical anomaly and be localized by the MWT. The third source (#3), beneath the NW side of the summit (Fig. 6), is near the main convergence of flow inside the summit area of the hydrothermal structure. The fourth source (#4) is spatially less well constrained. However, it is also at the intersection between two water flow paths: an eastward water flow from the west summit flank and a westward flow from the lower part of the east flank (Fig. 6). The fifth source (#5) is found on the SE boundary of the main water flow structure flowing westward. As stated by Yasukawa et al. (2003), the water flow inside Waita volcano is westward and controlled by the regional Takenoyu fault. The depths calculated by MWT of the SP data show that 4 of the 5 sources (#1, #3, #4, and #5) are found in the shallowest part of this westward flow. All are along the main flow direction and/or at the intersection of converging water flows, which likely supply the hydrothermal system.

On Masaya volcano, 6 groups of depths calculated by MWT characterize 6 sources in 2007 and 2008. The horizontal position and depths of these sources are very consistent between 2007 and 2008 (Fig. 7, Table 4), with a horizontal coefficient correlation (r_x^2) of 0.998 and a vertical coefficient correlation (r_z^2) of 0.81. Calculated water depths show a constant northward flow on the north flank of Nindiri cone and a southward flow on the south flank. The calculated depths (Table 4) indicate that, during 2007 and 2008, the water table is shallow (mean of 92 ± 34 m below the topographic surface). In 2004, MacNeil et al. (2007) made transient electromagnetic measurements through the caldera, including a profile across Nindiri cone (Fig. 1). Their study showed the presence of a low resistivity (<103 Ω m) layer which they inferred as the water table (Fig. 7). This TEM data shows a very similar trend with the water table becoming progressively shallower with increasing elevation. Although there is some discrepancy between the TEM modelled water table and the MWT calculated depths, when the mean depths (and uncertainties) from both methods are compared (Table 5), the depths of the water tables are indistinguishable.

Table 5
Comparison of water depths determined by multi-scale wavelet tomography of self-potential profiles and TEM models on Masaya volcano. **σ** is one standard deviation. TEM water model from MacNeil et al. (2007).

Method	Elevation a.s.l. (m)	South flank	North flank	Upper North flank	Lower North flank
MWT	Mean	400	333	341	297
	σ	80	63	25	60
TEM	Mean	256	271	343	200
	σ	67	85	28	16
	Difference	144	62	−2	97

As with all geophysical methods, especially potential field techniques, there are a number of limitations that must be considered in the application of multi-scale wavelet tomography (Sailhac and Marquis, 2001). MWT on self-potential data cannot uniquely determine the nature of the object associated with the SP anomaly and calculated depth. As is commonly the case with many inverse models, MWT assumes a homogeneous medium, which is a significant simplification. It is therefore important that self-potential surveys be made in conjunction with electrical tomography or electro-magnetic surveys to characterize the principle resistivity structures and how they are associated with the MWT-calculated depths. Multi-scale wavelet tomography of SP data has the advantage of being a rapid signal analysis technique which allows one to obtain reproducible results. As shown by this study, MWT on SP data can be used even on a noisy signal; the accuracy is good for a SNR up to 5, although there is a decrease in accuracy with increasing source depth. However, at relatively shallow depths (e.g., 100 m below the surface), the MWT can efficiently localize the source even with SNR up to 20%. When a combination of at least four different wavelets of the Poisson kernel family is used, it becomes possible to increase the depth accuracy, to reduce the number of artefacts and thus the uncertainty on the calculated depth. Using four wavelets to calculate the mean depth allows us to obtain a good accuracy, even with increasing noise and depth of the source (Table 3). Finally, the accurate depth calculations from MWT of self-potential data, when applied to time-series data, may be used to determine vertical change in the water flow.

7. Conclusion

This study demonstrates that multi-scale wavelet tomography, based on the Poisson wavelet family and applied to self-potential data, can reproducibly locate the boundaries of hydrothermal and hydrological structures; the MWT-calculated depths for Stromboli, Waita and Masaya volcanoes correlate well with structures identified by independent geophysical methods. Analyses of a range of synthetic models in homogenous and heterogeneous mediums show the accuracy of MWT-calculated depths even with signal/noise ratio reaching 5 (20%). Uncertainties in the results increase with greater depth, however, the MWT can still localize the source within

reasonable errors (Table 3). Traditionally, a SP survey a few km in length (e.g., profiles used in this study) can be made in a few days and complete data processing by MWT can be done in a single day. The vertical accuracy is sufficient to locate the top of the main hydrological structures, which is generally considered to be the main source of electric generation. Thus MWT may help to optimize drilling in the case of geothermal exploration. When applied to self-potential data from active volcanoes, MWT-derived depths can characterize the hydrothermal and/or hydrological systems and their relationship to the underlying magmatic plumbing system. Multi-scale wavelet tomography analysis of time-series self-potential data has the possibility to significantly improve volcano monitoring by accurately determining changes in the hydrothermal system which may be precursors of imminent volcanic activity.

Acknowledgements

This research was supported by a NSERC Discovery grant to G. Williams-Jones. We thank K. Simpson and P. Labazuy for their constructive comments. Many thanks to INETER and the Parque Nacional Volcan Masaya for their continued support in Nicaragua. This work would never have been possible without the help of A. Finizola, K. Yasukawa, C. Connor and R. MacNeil who graciously shared their data. Many thanks to the reviewers for their constructive comments.

References

Aizawa, K., Uyeshima, M., Nogami, K., 2008. Zeta potential estimation of volcanic rocks on 11 island arc-type volcanoes in Japan: implication for the generation of local Self-potential anomalies. J. Geophys. Res. 113, B02201. doi:10.1029/2007JB005058.

Barde-Cabusson, S., Finizola, A., Revil, A., Ricci, T., Piscitelli, S., Rizzo, E., Angeletti, B., Balasco, M., Bennati, L., Byrdina, S., Carzaniga, N., Crespy, A., Di Gangi, F., Morin, J., Perrone, A., Rossi, M., Roulleau, E., Suski, B., Villeneuve, N., 2009. New geological insights and structural control on fluid circulation in La Fossa cone (Vulcano, Aeolian Islands, Italy). J. Volcanol. Geotherm. Res. 185 (3), 231–245.

Battaglia, M., Troise, C., Obrizzo, F., Pingue, F., De Natale, G., 2006. Evidence for fluid migration as the source of deformation at Campi Flegrei caldera (Italy). Geophys. Res. Lett. 33, L01307. doi:10.1029/2005GL024904.

Cooper, G.R.J., 2006. Interpreting potential field data using continuous wavelet transforms of their horizontal derivatives. Comp. Geosci. 32 (7), 984–992.

Corwin, R.F., Hoover, D.B., 1979. Self-potential method in geothermal-exploration. Geophysics 44 (2), 226–245.

Crespy, A., Revil, A., Linde, N., Byrdina, S., Jardani, A., Bolève, A., Henry, P., 2008. Detection and localization of hydromechanical disturbance in a sandbox using the self-potential method. J. Geophys. Res. 113 (B01205). doi:10.1029/2007JB005042.

Fedi, M., Quarta, T., 1998. Wavelet analysis for the regional-residual and local separation of potential field anomalies. Geophys. Prospect. 46 (5), 507–525.

Fedi, M., Primiceri, R., Quarta, T., Villani, A.V., 2004. Joint application of continuous and discrete wavelet transform on gravity data to identify shallow and deep sources. Geophys. J. Int. 156 (1), 7–21.

Fedi, M., Paoletti, V., Rapolla, A., 2005. The role of multilevel data in potential field interpretation. Comp. Geosci. 31 (6), 681–688.

Finizola, A., Sortino, F., Lenat, J.F., Valenza, M., 2002. Fluid circulation at Stromboli volcano (Aeolian Islands, Italy) from self-potential and CO_2 surveys. J. Volcanol. Geotherm. Res. 116 (1–2), 1–18.

Finizola, A., Sortino, F., Lenat, J.F., Aubert, M., Ripepe, M., Valenza, M., 2003. The summit hydrothermal system of Stromboli. New insights from self-potential, temperature, CO_2 and fumarolic fluid measurements, with structural and monitoring implications. Bull. Volcanol. 65 (7), 486–504.

Finizola, A., Revil, A., Rizzo, E., Piscitelli, S., Ricci, T., Morin, J., Angeletti, B., Mocochain, L., Sortino, F., 2006. Hydrogeological insights at Stromboli volcano (Italy) from geoelectrical, temperature, and CO_2 soil degassing investigations. Geophys. Res. Lett. 33, L17304. doi:10.1029/2006GL026842.

Gibert, D., Pessel, M., 2001. Identification of sources of potential fields with the continuous wavelet transform: application to self-potential profiles. Geophys. Res. Lett. 28 (9), 1863–1866.

Gillot, P.Y., Keller, J., 1993. Radiochronological dating of Stromboli. Acta Vulcanol. 3, 69–77.

Grossmann, A., Morlet, J., 1984. Decomposition of hardy functions into square integrable wavelets of constant shape. Siam J. Math. Anal. 15 (4), 723–736.

Hornig-Kjarsgaard, I., Keller, J., Koberski, U., Stadlbauer, E., Francalanci, L., Lenhart, R., 1993. Geology, stratigraphy and volcanological evolution of the island of Stromboli, Aeolian Arc Italy. Acta Vulcanol. 3, 21–68.

Ikeda, Y., 1979. Active fault systems of the Quaternary volcanic region in the central part of Oita Prefecture, Kyushu district, southwest Japan. J. Geog. Soc. Japan 52, 10–29.

Ishido, T., Mizutani, H., 1981. Experimental and theoretical basis of electrokinetic phenomena in rock–water systems and its applications to geophysics. J. Geophys. Res. 86, 1763–1775.

Jardani, A., Dupont, J.P., Revil, A., 2006. Self-potential signals associated with preferential groundwater flow pathways in sinkholes. J. Geophys. Res. 111 (B09204). doi:10.1029/2005JB004231.

Jouniaux, L., Bernard, M.L., Zamora, M., Pozzi, J.P., 2000. Streaming potential in volcanic rocks from Mount Pelee. J. Geophys. Res. 105 (B4), 8391–8401.

Kamata, H., 1989. Volcanic and structural history of the Hohi volcanic zone, Central Kyushu. Japan. Bull. Volcanol. 51 (5), 315–332.

Kawamura, M., 1985. On the thermal structure of the geothermal field in Mt Waita area, central Kyushu, Japan. Rep. Geol. Surv. Japan 264, 115–142.

Lénat, J.F., 2007. Retrieving self-potential anomalies in a complex volcanic environment: an SP/elevation gradient approach. Near Surf. Geophys. 5 (3), 161–170.

MacNeil, R.E., Sanford, W.E., Connor, C.B., Sandberg, S.K., Diez, M., 2007. Investigation of the groundwater system at Masaya Caldera, Nicaragua, using transient electromagnetics and numerical simulation. J. Volcanol. Geotherm. Res. 166 (3–4), 217–232.

Minsley, B.J., Sogade, J., Morgan, F.D., 2007. Three-dimensional source inversion of self-potential data. J. of Geophys. Res. Solid Earth 112 (B02202). doi:10.1029/2006JB004262.

Moreau, F., Gibert, D., Holschneider, M., Saracco, G., 1997. Wavelet analysis of potential fields. Inv. Prob. 13 (1), 165–178.

Moreau, F., Gibert, D., Holschneider, M., Saracco, G., 1999. Identification of sources of potential fields with the continuous wavelet transform: basic theory. J. Geophys. Res. 104 (B3), 5003–5013.

Pasquaré, G., Francalanci, L., Garduno, V.H., Tibaldi, A., 1993. Structure and geologic evolution of the Stromboli volcano. Aeolian Island Italy Acta. Vulcanol. 3, 79–89.

Patella, D., 1997. Introduction to ground surface self-potential tomography. Geophysic. Prospect. 45, 653–681.

Revil, A., Schwaeger, H., Cathles III, L.M., Manhardt, P.D., 1999. Streaming potential in porous media 2. Theory and application to geothermal systems. J. Geophys. Res. 104 20,033–20,048.

Revil, A., Finizola, A., Sortino, F., Ripepe, M., 2004. Geophysical investigations at Stromboli volcano, Italy: implications for ground water flow and paroxysmal activity. Geophys. J. Int. 157 (1), 426–440.

Roche, O., Wyk de Vries, B.V., Druitt, T.H., 2001. Sub-surface structures and collapse mechanisms of summit pit craters. J. Volcanol. Geotherm. Res. 105 (1–2), 1–18.

Rymer, H., Wyk de Vries, B.V., Stix, J., Williams-Jones, G., 1998. Pit crater structure and processes governing persistent activity at Masaya Volcano. Nicaragua. Bull. Volcanol. 59 (5), 345–355.

Sailhac, P., Marquis, G., 2001. Analytic potentials for the forward and inverse modeling of SP anomalies caused by subsurface fluid flow. Geophys. Res. Lett. 28 (9), 1851–1854.

Sailhac, P., Galdeano, A., Gilbert, D., Moreau, F., Delor, C., 2000. Identification of sources of potential fields with the continuous wavelet transform: complex wavelets and application to aeromagnetic profiles in French Guiana. J. Geophys. Res. 105 (B8) 19,455–19,475.

Saracco, G., Labazuy, P., Moreau, F., 2004. Localization of self-potential sources in volcano-electric effect with complex continuous wavelet transform and electrical tomography methods for an active volcano. Geophys. Res. Lett. 31 (12), L12610.

Saracco, G., Moreau, F., Mathé, P.-E., Hermitte, D., Michel, J.-M., 2007. Multi-scale tomography of buried magnetic structures: its use in the localization and characterization of archeological structures. Geophys. J. Int. 1, 87–103.

Walker, J.A., Williams, S.N., Kalamarides, R.I., Feigenson, M.D., 1993. Shallow open-system evolution of basaltic magma beneath a subduction zone volcano: the Masaya Caldera Complex, Nicaragua. J. Volcanol. Geotherm. Res. 56, 379–400.

Widarto, D.S., Kawahigashi, K., Katsura, I., Nishimura, S., Mogi, T., Ehara, S., Shimoizumi, M., Nishida, J., Kusunoki, K., Suzuki, K., Fujimitsu, Y., Higashi, S., Jomori, A., Matayoshi, S., 1992. Geothermal significance of CSMT–TDEM joint surveys in the vicinity of Waita volcano—the Hohi region, central Kyushu. Proceedings 86th Society Exploration Geophysics Japan, pp. 276–280.

Williams, S.N., 1983. Plinian airfall deposits of basaltic composition. Geology 11, 211–214.

Williams-Jones, G., Rymer, H., Rothery, D.A., 2003. Gravity changes and passive SO_2 degassing at the Masaya caldera complex, Nicaragua. J. Volcanol. Geotherm. Res. 123 (1–2), 137–160.

Yasukawa, K., Mogi, T., Widarto, D., Ehara, S., 2003. Numerical modeling of a hydrothermal system around Waita volcano, Kyushu, Japan, based on resistivity and Self-potential survey results. Geothermics 32 (1), 21–46.

Zlotnicki, J., Nishida, Y., 2003. Review on morphological insights of self-potential anomalies on volcanoes. Surv. Geophys. 24 (4), 291–338.